

# Influence of microstructure topology on the mechanical properties of powder compacted materials

Lai, Chang Quan; Seetoh, Ian

2021

Lai, C. Q., & Seetoh, I. (2021). Influence of microstructure topology on the mechanical properties of powder compacted materials. *International Journal of Mechanical Sciences*, 198, 106353-. doi:10.1016/j.ijmecsci.2021.106353

<https://hdl.handle.net/10356/146719>

<https://doi.org/10.1016/j.ijmecsci.2021.106353>

---

© 2021 Elsevier Ltd. All rights reserved. This paper was published in *International Journal of Mechanical Sciences* and is made available with permission of Elsevier Ltd.

*Downloaded on 05 Apr 2024 12:52:43 SGT*

# **Influence of Microstructure Topology on the Mechanical Properties of Powder Compacted Materials**

Chang Quan Lai<sup>1,\*</sup> & Ian Seetoh<sup>1</sup>

<sup>1</sup>*Temasek Laboratories, Nanyang Technological University, 50 Nanyang Drive, Singapore 637553*

\*cqlai@ntu.edu.sg

Keywords: Particles, Lattices, Sinter, Relative Density, Powder Compacted, Powder Metallurgy, Additive Manufacturing, Powder Bed 3D Printing

## **ABSTRACT**

Powder compaction is an important technique for fabricating engineering materials as it offers good resolution and is compatible with complex stoichiometry and geometries. It forms the basis of important manufacturing processes such as powder bed 3D printing, powder metallurgy and metal injection moulding. However, a major disadvantage is that the presence of porosity in the resultant material can lead to a drastic deterioration of its mechanical properties. To improve the stiffness and strength of these powder compacts, it is imperative to pinpoint the main cause of these weakening effects. Here, we attempt to do so by examining the mechanics of different topologies that the microstructures of powder compacted materials can adopt. General structure – property relationships were first derived for (i) compression/stretch – dominated (CD) (ii) compression, shear and bending (CSB) and (iii) compression, shear and joint rotation (CSR) topologies, for the range of relative densities between 0 and ~ 0.9. Using the Face-Centered Cubic (FCC), Body-Centered Cubic (BCC) and 3D Anti-Tetrachiral (3ATC) geometries to represent the CD, CSB and CSR topologies respectively, the

analytical and simulated relative stiffness vs. relative density and relative strength vs. relative density trends were compared against experimental data in the literature. It was found that the mechanical properties of powdered materials typically fall within an exclusive range of values exhibited by the 3ATC lattice, which is much lower than that expected of FCC and BCC lattices. A closer examination of the analytical equations indicated that the low modulus of 3ATC lattices and powder compacted materials is caused by joint (*i.e.* particulate) rotation, while their weak strength is the result of thin beams, which manifest as narrow neck-like interparticle connections in powder compacted materials. These results are supported by previous studies, which showed that powder compacted materials have eccentric microstructures similar to 3ATC unit cells and the compression of granular material usually results in extensive particulate rotations. Higher coordination number of the particles is expected to reduce these rotations, thus illuminating the strategy for improving the modulus of powder compacted materials. The material strength, on the other hand, has already been shown to improve with a thickening of the neck regions, which can be achieved through higher sintering temperature, compressive pressure and/ or longer compaction time.

## 1. INTRODUCTION

Cellular solids are an important class of engineering materials because they offer unique combinations of properties such as lightweight characteristics [1–3], good load bearing capabilities [4–6] and excellent energy absorption efficiencies [7–9]. Low relative density ( $< 20\%$ ) materials are often used as acoustic [10] and shock absorbers [7,8,11] or space frames for buildings and vehicular bodies [4,12,13]. On the other hand, large relative density cellular solids ( $\geq 0.2$ ) possess moderate stiffness and strength, as well as energy absorption characteristics that lie between the extremes of solid and low relative density materials [14–17]. These materials are important for applications such as biomedical implants used in reconstructive surgery [18–20] and tissue engineering [21].

There are several methods of producing porous cellular materials, including direct foaming (introduction of air/ gas bubbles) [16,22,23], dealloying of solid solutions (selective dissolution of one metal in an alloy to form pores) [24,25], 3D printing (layer by layer addition of material at precise spatial positions) [26–30] and powder compaction, where loose particles in the form of fine powder are fused together to form a desired geometry through the application of heat and/ or pressure [6,31,32]. Spacer particles, which are removed in a subsequent processing step, can be added to the functional particles to increase the porosity of the part [21].

Powder compaction is an important technique that forms the basis of processes such as metal injection moulding [33], powder metallurgy [34,35], hot isostatic pressing [36,37] and powder bed 3D printing, which includes selective laser sintering (SLS) [26,38], selective laser melting (SLM) [39] and electron beam melting (EBM) [27]. In powder bed 3D printing, selective regions in a thin layer of powder are made to coalesce using intense heat generated by a laser or electron beam. By successively depositing and sintering/ melting powder layers, a coherent 3D part can be produced.

Powder compaction can be used to produce parts with complex geometries [26], intricate details (*i.e.* fine resolution) [33] and complicated stoichiometry [38]. One major drawback, however, is a rapid deterioration of the mechanical properties of the parts in the presence of porosity [32]. For instance, the ultimate tensile strength of thermoplastic polyurethane (TPU) powder sintered using SLS was found to fall by 72% when the relative density decreased by 8%, from 0.95 to 0.87 [40]. Because of this, functional components produced by powder compaction are currently limited to solid parts that have been densified to relative densities greater than 95% [33].

To fully exploit the advantages of powder compaction for the production of porous materials, the mechanical properties of these parts have to be improved significantly. An important first step towards this end is to identify the root cause behind these inferior mechanical properties which, despite decades of powder compaction research, remains unclear. In the following, we seek to clarify this by considering the various microstructure topologies that powder compacted materials can adopt. The mechanical properties of these topologies are then examined through analytical and numerical means, before comparing them against experimental values reported in the literature to gain useful insights.

## 2. GENERAL MODEL

The physical and mechanical properties of powder compacted materials will be examined in this section. We begin by considering the 3 basic types of geometries the microstructures can adopt. These topologies are named according to the deformations that the microstructure experiences in the presence of a load – (i) the compression-dominated (CD) design (also known as stretch-dominated design) (ii) the compression, shear and bending (CSB) design and (iii) compression, shear and joint rotation (CSR) design. General structure-property relationships for the 3 topologies will first be derived. These analytical equations are expected to be valid for  $\rho/\rho_s \leq 0.9$ , beyond which pore morphologies and variations in local density are expected to supersede the importance of beam arrangements in determining lattice mechanics [15,41,42].

To validate our analysis, specific geometrical parameters for the Face-Centered Cubic (FCC; also commonly known as Octet Truss [4,43]) (Fig. 1a), Body-Centered Cubic (BCC) (Fig. 1b) and 3D Anti-Tetrachiral (3ATC) (Fig. 1c) lattices will be applied to the general solutions of the CD, CSB and CSR topologies respectively. These geometry-specific analytical solutions will then be compared to data obtained from finite element simulations (COMSOL 5.3a), as well as experiments from the literature, in the next section, under “Results”. FCC  $\langle 111 \rangle$ , BCC  $\langle 100 \rangle$  and 3ATC  $\langle 100 \rangle$  lattices were selected to represent the various topologies as these geometries and orientations had previously been observed in self-assembled particles [44–46]. Since the packing of the particles is a primary factor in determining the microstructure of powder compacted materials, these geometries are, therefore, more relevant to the present study.

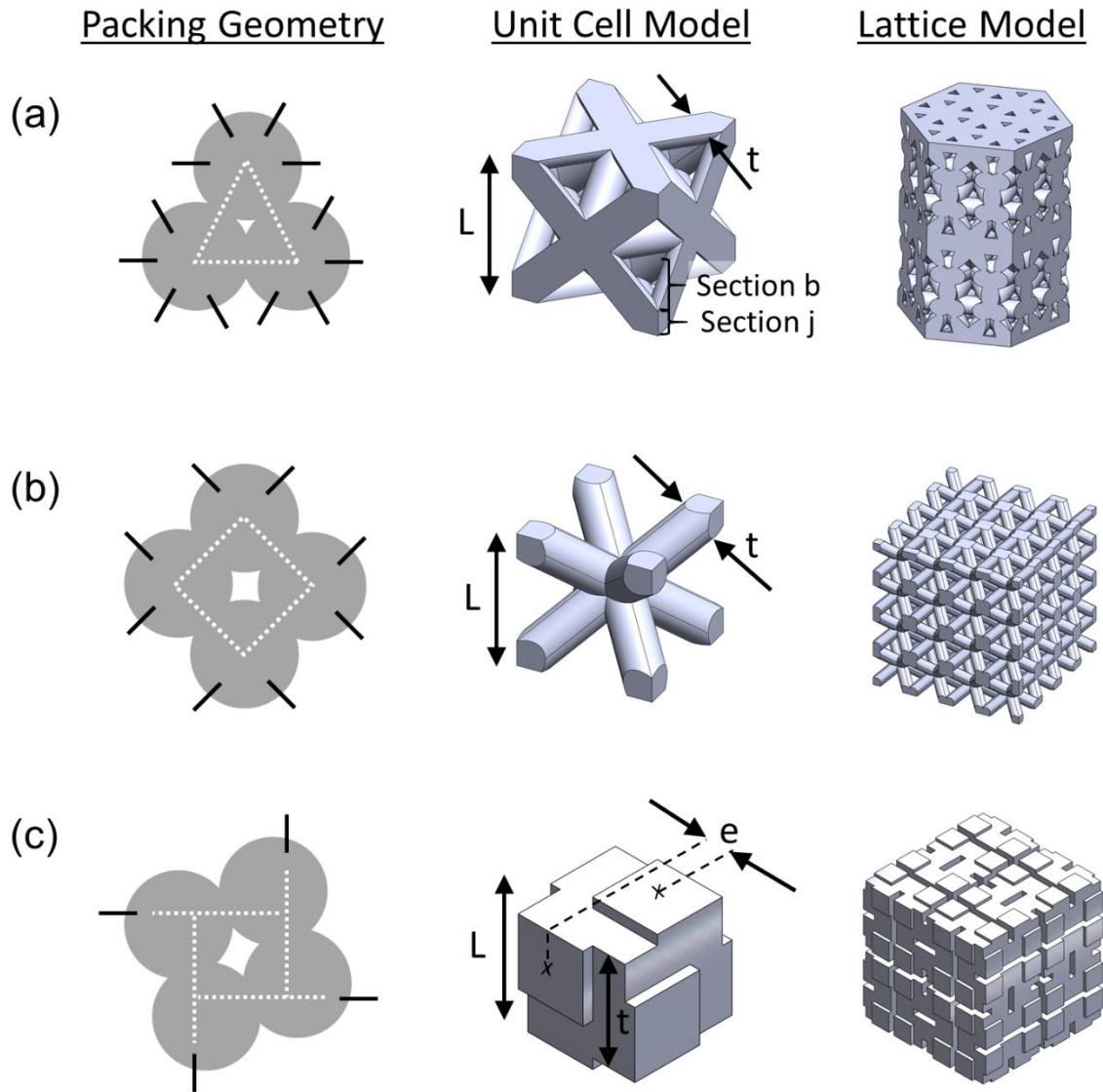


Figure 1: Schematic diagrams showing the arrangement of powder compacted particles, as well as the corresponding idealized unit cell and idealized lattice designs for the (a) Face-Centered Cubic (FCC)/ Octet Truss  $\langle 111 \rangle$  packing geometry; representative of the CD topology (b) Body-Centered Cubic (BCC)  $\langle 100 \rangle$  packing geometry; representative of the CSB topology (c) 3D Anti-Tetrachiral (3ATC)  $\langle 100 \rangle$  packing geometry; representative of the CSR topology. The white dotted lines in the leftmost diagrams represent the lines of action for external forces, while the black lines indicate the locations where the particles join up with their other neighbours.

## 2.1 Relative Density

The unit cells considered in this analysis are 3D, symmetric about the 3 cartesian axes and consist of beams and joints arranged within a space of  $L \times L \times L$  (Fig. 1). The volume of

each joint is proportional to  $t \times t \times t$ , while the length of each beam is proportional to  $(L - \gamma t)$ , where  $\gamma$  is a constant that can be calculated based on the lattice geometry. For instance, in the case of the BCC structure, the length of the beam is approximately  $\sqrt{3}L - 2t$  and therefore,  $\gamma = 2/\sqrt{3}$ . The cross-section of the beam is proportional to  $t \times t$  for the CD and CSB topologies and  $(t - e) \times (t - e)$  for the CSR topology. The relative density,  $\rho/\rho_s$ , of the CD and CSB geometries can then be given by [4]

$$\frac{\rho}{\rho_s} = A \left[ \left( \frac{t}{L} \right)^2 - D \left( \frac{t}{L} \right)^3 \right], \quad (1)$$

where  $A$  and  $D$  are constants that can be derived from the geometry of the unit cell (Table 1).

For the CSR topology, the relative density can similarly be derived to be [9,47]

$$\frac{\rho}{\rho_s} = A \left( \frac{t}{L} - \frac{e}{L} \right)^2 \left( 1 - \gamma \frac{t}{L} \right) + D \left( \frac{t}{L} \right)^3. \quad (2)$$

Table 1: Properties of the lattices used for analytical calculations and finite element simulations. The relative density of the FCC/ Octet Truss and BCC lattice was modulated by varying  $t/L$ , while that for the 3ATC was varied using different  $L$  and  $e$  separately. The Poisson's ratio used was  $\nu \sim 0.4$  for all designs.

Design	Coordination Number	Loading	$A$	$D$	$\gamma$	$e$	$t$	$L$
FCC/ Octet Truss	12	Symmetric	17	1.18	1.41	-	-	-
BCC	8		6.9	0.87	1.15	-	-	-
3ATC	6	Eccentric	6	1	1	1.5	3	vary
						vary	3	0.6

## **2.2 Compression/ Stretch-Dominated (CD) Topology**

### **2.2.1 Relative Stiffness**



Under the influence of a load, a material would, at the minimum, be subjected to compressive/ tensile deformation. The compressive strain,  $\varepsilon_{stretch}$ , can be derived using

$$\varepsilon_{stretch} = \frac{\Delta_b + \Delta_j}{L}, \quad (3)$$

where  $\Delta_b$  refers to the displacement in the beams parallel to the loading axis (*e.g.* section  $b$  in Fig. 1) and  $\Delta_j$  refers to the displacement in the joint region (*e.g.* section  $j$  in Fig. 1). Because the effective loading area at section  $j$  is typically much larger than that at section  $b$ , therefore, as a first order approximation, we assume  $\Delta_b \gg \Delta_j$  to simplify the calculations. From Fig. 1,  $\Delta_b$  can be calculated as

$$\Delta_b \propto \frac{F(L-2t)}{t^2 E_s}, \quad (4)$$

where  $F$  is the force on a unit cell and  $E_s$  is the Young's modulus of the constitutive material of the structure.

Since the stiffness of the overall structure,  $E$ , is given as

$$E = \frac{\sigma}{\varepsilon_{stretch}}, \quad (5)$$

and the effective stress on the structure,  $\sigma$ , is  $F/L^2$ , Eq. (5) can be rearranged to give the material-independent parameter of relative stiffness,  $E/E_s$ , as

$$\frac{E}{E_s} = \frac{1}{k_{stretch} \left[ \frac{1}{\left(\frac{t}{L}\right)^2} - \frac{2}{\left(\frac{t}{L}\right)} \right]}, \quad (6)$$

where  $k_{stretch}$  is a constant. If we impose the condition that  $E/E_s = 1$  when  $\rho/\rho_s = 1$ ,  $k_{stretch}$  can be found. As an example, using Eq. (1) and the values of  $A$  and  $D$  for the FCC/ Octet Truss structure (Table 1), it can be observed that  $\rho/\rho_s = 1$  when  $t/L = 0.303$ . For this value of  $t/L$ ,  $E/E_s = 1$ , so that Eq. (6) yields  $k_{stretch} = 0.233$ .

### 2.2.2 Relative Strength

Under uniaxial loading, some beams in a compression – dominated structure may nevertheless exhibit limited buckling (Fig. 2a and 2b) [42]. These deformations do not influence the relative stiffness appreciably at small strains. However, the bending stress,  $\sigma_{bend}$ , has to be accounted for when considering the failure stress of the structure,  $\sigma_f$ , since its magnitude can be similar to that of compressive/ tensile stresses,  $\sigma_{stretch}$ . Since  $\sigma_{stretch}$  and  $\sigma_{bend}$  are applied along the length of a beam and are parallel to each other, the structure will begin to fail when the sum of these stresses exceeds the yield/fracture stress of the constitutive material,  $\sigma_s$ . In other words,

$$\sigma_s = \sigma_{stretch,f} + \sigma_{bend,f}, \quad (7)$$

where 
$$\sigma_{stretch,f} = \alpha_{stretch} \frac{F_f}{t^2} \quad (8)$$

and 
$$\sigma_{bend,f} = \alpha_{bend} \frac{F_f(L-\gamma t)}{t^3}. \quad (9)$$

$\alpha_{stretch}$  and  $\alpha_{bend}$  are proportionality constants and  $F_f$  refers to the critical force required to induce failure in the structure. Since  $F_f = \sigma_f L^2$ , therefore, the relative strength,  $\sigma_f/\sigma_s$ , can be derived as

$$\frac{\sigma_f}{\sigma_s} = \frac{1}{\frac{(\alpha_{stretch} - \gamma \alpha_{bend})}{(t/L)^2} + \frac{\alpha_{bend}}{(t/L)^3}}, \quad (10)$$

### 2.2.3 Low Relative Density

At low relative densities (*i.e.*  $t/L \ll 1$ ), Eq. (1) reduces to

$$\frac{\rho}{\rho_s} \propto \left(\frac{t}{L}\right)^2. \quad (11)$$

For the relative stiffness shown in Eq. (6),  $1/(t/L)^2 \gg 1/(t/L)$ , so

$$\frac{E}{E_s} \propto \left(\frac{t}{L}\right)^2, \quad (12)$$

which, from Eq. (11), is equivalent to

$$\frac{E}{E_s} \propto \frac{\rho}{\rho_s}. \quad (13)$$

This result is consistent with that of previous analyses conducted for low relative density FCC/Octet Truss structures [4,12].

Similarly, for Eq. (10), the buckling term,  $\alpha_{bend}/(t/L)^3$ , dominates in the denominator so that

$$\frac{\sigma_f}{\sigma_s} \propto \left(\frac{t}{L}\right)^3 \quad (14)$$

which can be re-written as

$$\frac{\sigma_f}{\sigma_s} \propto \left(\frac{\rho}{\rho_s}\right)^{1.5} \quad (15)$$

It should be noted from Eq. (10), however, that the  $t/L$  and therefore,  $\rho/\rho_s$ , required to observe the above result depends on the relative magnitude of the coefficients,  $\alpha_{stretch} - \gamma\alpha_{bend}$ , and  $\alpha_{bend}$ . The greater the value of  $(\alpha_{stretch} - \gamma\alpha_{bend})/\alpha_{bend}$ , the smaller  $\rho/\rho_s$  will have to be for the buckling term,  $\alpha_{bend}/(t/L)^3$ , to dominate. Based on literature reports, it would appear that  $(\alpha_{stretch} - \gamma\alpha_{bend})/\alpha_{bend}$  is generally a large value, as the result in Eq. (15) had, thus far, only been observed for  $\rho/\rho_s \leq 0.002$  [3].

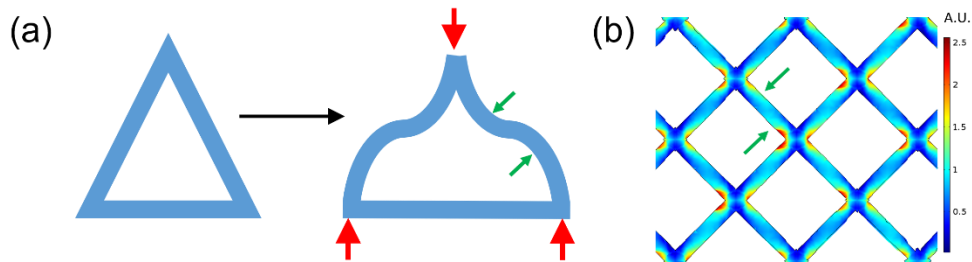


Figure 2: (a) Schematic illustration of part of the FCC structure (*a.k.a.* Octet Truss) undergoing compression/ stretch - dominated deformation. Red arrows represent the external forces acting on the structure, while green arrows highlight the regions under compression due to the buckling of the beams. (b) Simulation result (COMSOL 5.3a) showing the stress distribution of a 2D slice within an FCC structure undergoing uniaxial compression. The green arrows highlight the elevated bending stresses as expected. Note that the horizontal beams cannot be seen here as they are out of plane. A.U. – Arbitrary Units.

## **2.3 Compression, Shear & Bending (CSB) Topology**

### **2.3.1 Relative Stiffness**

On top of compression, a unit cell under load can also experience bending deformation with accompanying shear strain. The mechanics of beam bending in lattices with small relative densities had been analysed by Gibson and Ashby previously [41], and it was shown that the effective lattice strain in these bending - dominated structures,  $\varepsilon_{bend}$ , can be expressed as

$$\varepsilon_{bend} \propto \frac{F(L-\gamma t)^3}{E_s I L}, \quad (16)$$

where  $I$  is the second moment of area, which is proportional to  $t^4$ .

For short and thick beams that are usually present in large relative density lattices, the lattice strain caused by shear stresses,  $\varepsilon_{shear}$ , may not be negligible, and is derived using the Timoshenko beam theory to be [48,49]

$$\varepsilon_{shear} \propto \frac{F(L-\gamma t)}{E_s t^2 L}. \quad (17)$$

The tensile/ compressive lattice strain caused by  $F$  on the lattice is given previously in Eq. (2) – Eq. (4). The stiffness of a CSB structure,  $E$ , can therefore be expressed as

$$E = \frac{\sigma}{\varepsilon_{bend} + \varepsilon_{shear} + \varepsilon_{stretch}}, \quad (18)$$

which can be re-written as

$$\frac{E}{E_s} = \frac{1}{C_{bend} + C_{shear} + C_{stretch}}, \quad (19)$$

where

$$C_{bend} = k_{bend} \frac{(1 - \nu \frac{t}{L})^3}{(\frac{t}{L})^4}, \quad (20)$$

$$C_{shear} = k_{shear} (1 + \nu) \left[ \frac{1}{(\frac{t}{L})^2} - \frac{\nu}{(\frac{t}{L})} \right], \quad (21)$$

and

$$C_{stretch} = k_{stretch} \left[ \frac{1}{(\frac{t}{L})^2} - \frac{2}{(\frac{t}{L})} \right]. \quad (22)$$

$k_{bend}$ ,  $k_{shear}$  and  $k_{stretch}$  are the proportionality constants for bending, shearing and tensile/compressive contributions respectively and  $\nu$  refers to the Poisson's ratio. Previous findings for foams and lattices of similar topology at low relative densities (*i.e.*  $t/L \ll 1$ ) showed that  $E/E_s = (\rho/\rho_s)^2$  [2,3,11], and therefore,

$$k_{bend} = 1/A^2 \quad (23)$$

If it can be assumed that  $E/E_s = 1$  when  $\rho/\rho_s = 1$ , which occurs when  $t/L = 0.511$  for the BCC lattice, then the relationship between  $k_{stretch}$  and  $k_{shear}$  can be obtained as

$$k_{stretch} = 10 \left[ \frac{0.978}{A^2} + 1.55(1 + \nu)k_{shear} - 1 \right]. \quad (24)$$

### 2.3.2 Relative Strength

The most likely points of failure for CSB structures are the beam surfaces in the sections subjected to the highest bending moments (*e.g.* encircled region in Fig. 3). A beam element at these locations experiences the maximal bending stress, a compressive stress in a perpendicular direction, as well as shear stress (Fig. 3). The principal stresses,  $\sigma_{P1}$  and  $\sigma_{P2}$ , can therefore be expressed as [50]

$$\sigma_{P1,P2} = \sigma_{bend} \left[ \frac{1}{2} \left( 1 + \frac{\sigma_{stretch}}{\sigma_{bend}} \right) \pm \sqrt{\left[ \frac{1}{2} \left( 1 - \frac{\sigma_{stretch}}{\sigma_{bend}} \right) \right]^2 + \left( \frac{\sigma_{shear}}{\sigma_{bend}} \right)^2} \right], \quad (25)$$

where

$$\sigma_{bend} = \alpha_{bend} \frac{Ft(L-\gamma t)}{I}, \quad (26)$$

$$\sigma_{shear} = \alpha_{shear} \frac{F}{t^2}, \quad (27)$$

and

$$\sigma_{stretch} = \alpha_{stretch} \frac{F}{Lt}. \quad (28)$$

$\alpha$  refers to the proportionality constant for the deformation mode denoted in the subscript.

Since material failure occurs when  $\sigma_{Pl} \geq \sigma_s$ , using the Tresca criterion [51] and noting that the effective force causing lattice failure is  $F = \sigma_f L^2$ , the relative strength of a CSB structure can be expressed as

$$\frac{\sigma_f}{\sigma_s} = \alpha_{bend} \frac{\left(\frac{t}{L}\right)^3}{1-\gamma\left(\frac{t}{L}\right)} \left\{ \left[ \frac{1}{2} \left( 1 - \frac{\sigma_{stretch}}{\sigma_{bend}} \right) \right]^2 + \left( \frac{\sigma_{shear}}{\sigma_{bend}} \right)^2 \right\}^{-\frac{1}{2}}, \quad (29)$$

where

$$\frac{\sigma_{shear}}{\sigma_{bend}} = \alpha_{shear} \frac{1}{\frac{t}{L} - \gamma}, \quad (30)$$

and

$$\frac{\sigma_{stretch}}{\sigma_{bend}} = \alpha_{stretch} \frac{1}{\left(\frac{1}{t/L}\right)^2 - \frac{\gamma}{t/L}}. \quad (31)$$

### 2.3.3 Low Relative Density

For relative stiffness, when  $t/L \ll 1$ , it can be seen from Eq. (19) – (22) that the bending term,  $C_{bend}$ , dominates over  $C_{shear}$  and  $C_{stretch}$  due to its  $(t/L)^4$  denominator. Therefore,

$$\frac{E}{E_s} \propto \left( \frac{t}{L} \right)^4, \quad (32)$$

and from Eq. (11),

$$\frac{E}{E_s} \propto \left( \frac{\rho}{\rho_s} \right)^2. \quad (33)$$

Similarly, for relative strength, a small  $t/L$  would cause  $\sigma_{shear}/\sigma_{bend}$  and  $\sigma_{stretch}/\sigma_{bend}$  to approach 0 (*i.e.* bending stress dominates), so

$$\frac{\sigma_f}{\sigma_s} \propto \left(\frac{t}{L}\right)^3, \quad (34)$$

which is,

$$\frac{\sigma_f}{\sigma_s} \propto \left(\frac{\rho}{\rho_s}\right)^{1.5} \quad (35)$$

Once again, these results are consistent with previous derivations [41] and demonstrates that bending-dominated designs are basically CSB designs at low relative densities.

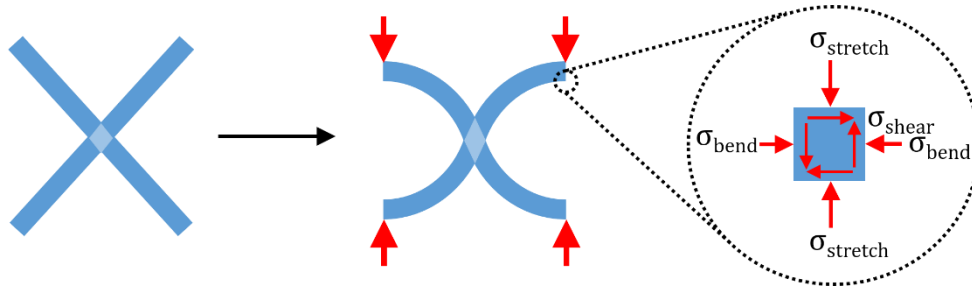


Figure 3: Schematic illustration of the BCC structure undergoing uniaxial deformation without joint (highlighted in light blue) rotation. Red arrows represent the external forces acting on the structure. An element in the beam is magnified to show the compressive, shear and bending stresses acting on it.

## **2.4 Compression, Shear & Joint Rotation (CSR) Topology**

### **2.4.1 Relative Stiffness**

Unlike the CD and CSB topologies, where loading forces are symmetrically applied, eccentric loading in CSR designs results in joint rotation (Fig. 4a) [9,47,52], with accompanying shear and compressive deformation. As with the case of FCC/ Octet Truss design, the buckling of the beams does not contribute appreciably to the lattice strain but will be important for the determination of the failure stress.

At low relative densities, the main contribution to the overall lattice strain of CSR structures arises from rotation of the joints [9]. In the elastic, small strain limit, the rotation angle of the joint,  $\theta$ , is correspondingly low. Applying the small angle approximation to the solutions developed previously [9,47], the effective lattice strain caused by joint rotation,  $\varepsilon_{rot}$ , can be obtained as

$$\varepsilon_{rot} \propto \frac{e\theta}{L}, \quad (36)$$

where

$$\theta \propto \frac{\sigma}{E_s} \frac{\left(\frac{L}{e}\right)^3}{\left(1-\frac{t}{L}\right)^2 \left(\frac{t}{e}-1\right)^4}. \quad (37)$$

The effective strain caused by shear stresses acting on the joints,  $\varepsilon_{shear}$ , can be derived as

$$\varepsilon_{shear} \propto \frac{\sigma}{E_s} (1 + \nu) \left(\frac{eL}{t^2}\right). \quad (38)$$

The compressive strain,  $\varepsilon_{stretch}$ , caused by normal stresses acting on the beam,  $\varepsilon_{stretch,b}$ , and the joint,  $\varepsilon_{stretch,j}$ , is found to be

$$\varepsilon_{stretch} = \varepsilon_{stretch,b} + \varepsilon_{stretch,j}, \quad (39)$$

where

$$\varepsilon_{stretch,b} \propto \frac{\sigma}{E_s} \frac{\left(1-\frac{t}{L}\right)}{\left(\frac{t-e}{L}\right)^2}, \quad (40)$$

and

$$\varepsilon_{stretch,j} = \frac{\sigma}{E_s} \left(\frac{L}{t}\right). \quad (41)$$

Unlike the case of CD topology, the compressive deformation of the joint is accounted for here since the joint can be large even at small relative densities and the loading area in section  $j$  may not necessarily be significantly larger than that of section  $b$ , as the cross-section of the horizontal beams is  $(t - e) \times (t - e)$ , which may be much smaller than that of the joint.



Since

$$E = \frac{\sigma}{\varepsilon_{rot} + \varepsilon_{shear} + \varepsilon_{stretch}}, \quad (42)$$

the relative stiffness of the eccentric structure can then be given as

$$\frac{E}{E_s} = \frac{1 - \frac{t}{L}}{\left[ k_{rot} e^2 \frac{(L-t)^2}{(t-e)^4} + k_{shear} (1+\nu) \left( \frac{e}{t} \right) \left( \frac{L}{t} - 1 \right) + k_{stretch} \left( \frac{L-t}{t-e} \right) + \frac{L}{t} - 1 \right]}, \quad (43)$$

where  $k$  refers to the proportionality constant for the respective deformation mode denoted in the subscript.

#### 2.4.2 Relative Strength

Failure of CSR structures are expected to take place when the maximum sum of bending and compressive stress in the beams, which are thinner and therefore, weaker than the joints, exceed the material strength *i.e.*  $\sigma_s \geq \sigma_{bend} + \sigma_{stretch}$  (Fig. 4b). Since the bending moment acting on the beams is proportional to  $Fe$  and distance of centroid to beam surface is  $(t - e)/2$ ,

$$\sigma_{bend} \propto \frac{Fe(t-e)}{I} = \frac{Fe}{(t-e)^3} \quad (44)$$

and

$$\sigma_{stretch} \propto \frac{F}{(t-e)^2}, \quad (45)$$

therefore, the relative strength can be obtained as

$$\frac{\sigma_f}{\sigma_s} = \left( \frac{e}{L} \right)^2 \frac{\left( \frac{t}{e} - 1 \right)^3}{\alpha_{bend} + \alpha_{stretch} \left( \frac{t}{e} - 1 \right)}. \quad (46)$$

where  $\alpha$  is a proportionality constant for the deformation mode denoted in the subscript.

From Eq. (2), (43) and (46), it can be seen that the physical and mechanical properties of CSR structures are dependent not just on the geometrical parameter of  $t/L$ , but also  $e/L$  and  $e/t$ . However, there are only 2 independent parameters, since  $e/L = t/L \times e/t$ . Therefore, for 3ATC lattices,  $\rho/\rho_s$  was varied in 2 ways to establish an upper and lower bound of their mechanical properties – (i) changing  $t/L$  while keeping  $e/t$  constant and (ii) changing  $e/t$  while keeping  $t/L$  constant.

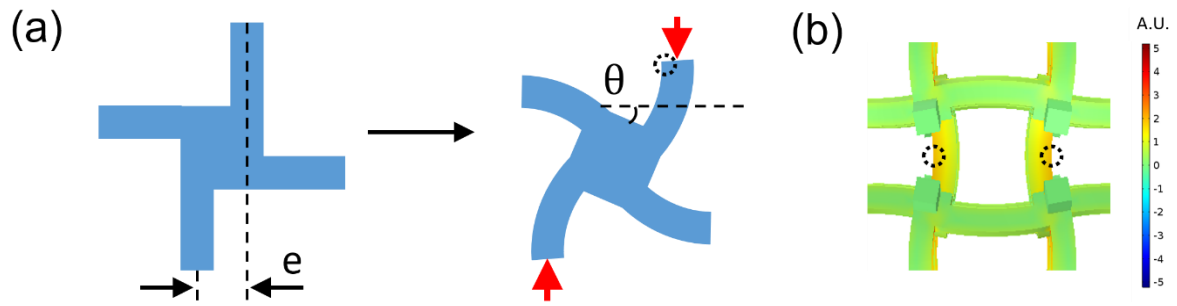


Figure 4: (a) Schematic illustration of a 3ATC subunit cell undergoing deformation. Red arrows represent the external forces acting on the structure, while the encircled region indicates the presence of the highest compressive stress. Note that the joint rotates by an angle of  $\theta$ . (b) Simulation result showing the stress distribution in a unit cell of the 3ATC lattice undergoing uniaxial compression. The regions experiencing maximum stress are circled. A.U. – Arbitrary Units.

### 3. RESULTS

#### 3.1 Relative Stiffness

Fig. 5 shows the simulated (solid lines) and analytical trends (broken lines) of  $E/E_s$  vs.  $\rho/\rho_s$  for the FCC/ Octet Truss, BCC and 3ATC lattices. Finite element simulations were performed on  $4 \times 4 \times 4$  lattices of the respective designs using the condition of stationary loading in COMSOL 5.3a. As can be observed, the fitting of the theoretical trends to the simulations is reasonably good (fitting parameters are shown in Table 2), indicating that the structure-property relationships derived in the preceding section are mostly valid.

Next, to ascertain if FCC/ Octet Truss & BCC are suitable representatives of the CD and CSB topologies respectively, we plotted the simulated values of alternative geometries, Simple Cubic (100) (CD) [9] and Kelvin Cell (*i.e.* tetrakaidecahedron) (CSB) [53], in Fig. 5 as well. It can be seen that the values of Simple Cubic (100) follow the trend of FCC (111) quite closely while that of Kelvin Cell adhered to the CSB trend initially before transitioning over to the CD trend for  $\rho/\rho_s > 0.2$ . This may be because parts of the Kelvin Cell densify rapidly with increasing beam width, resulting in compression-dominated deformation in these regions. This rapid densification is also the reason that very high relative densities were unobtainable for the Kelvin Cell.

Nevertheless, it is clear that  $E/E_s$  is generally highest for CD for a given  $\rho/\rho_s$ , followed closely by the CSB design. 3ATC, representative of the CSR design, on the other hand, exhibits very low  $E/E_s$  values (pink region). For  $\rho/\rho_s > 0.7$ , the range of possible  $E/E_s$  values widens rapidly, from as low as 0.1 to as high as the values for BCC lattices. The boundaries of the pink region are by no means the definitive limits of  $E/E_s$  values for 3ATC lattices, but they clearly illustrate that 3ATC lattices can have unique combinations of  $E/E_s$  and  $\rho/\rho_s$ , that are unattainable by CD and CSB designs.

Table 2: Independent fitting parameters for the analytical solutions (indicated by the respective equation numbers) shown in Fig. 6 and Fig. 8.

Design	$E/E_s$				$\sigma/\sigma_s$			
	Parameters			Eq. No.	Parameters			Eq. No.
	$k_{rot}$	$k_{shear}$	$k_{stretch}$		$\alpha_{bend}$	$\alpha_{shear}$	$\alpha_{stretch}$	
FCC	-	-	-	(6)	0.01	-	0.13	(10)
BCC	-	0.46	-	(19) - (22)	0.43	0.01	0.50	(29) - (31)
3ATC	8	0.7	0.8	(43)	0.1	-	1	(46)

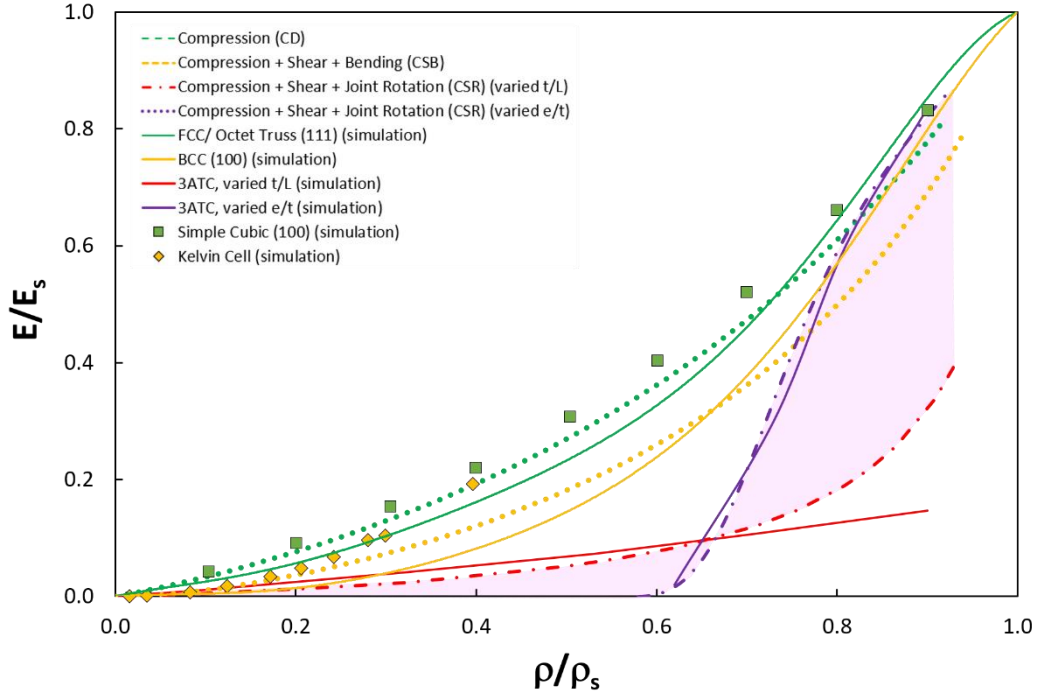


Figure 5: Simulated (solid lines) and fitted analytical trends (broken lines) of relative stiffness,  $E/E_s$ , vs. relative density,  $\rho/\rho_s$ , for the various lattices. Region highlighted in pink represents the range of possible  $E/E_s$  values for the general 3ATC geometry.

In Fig. 6, the experimental results of  $E/E_s$  vs.  $\rho/\rho_s$  for powder compacted materials obtained from the literature (black data points) are plotted against the analytical and simulated trends in Fig. 5. The results clearly show that the stiffness of powder compacted materials generally fall within the range of values exhibited by 3ATC lattices (pink region). It is worth noting, in particular, that the power law index for 3ATC can be very high (between 3 and 14) at large relative densities ( $> 0.4$ ), indicating that small increments of porosity can lead to drastic reductions in material stiffness, which is consistent with experimental observations involving powder compacted materials [31,32]. These results strongly suggest that the microstructures of powder compacted materials share similar deformation modes as the unit cell of 3ATC *i.e.* both belong to the CSR topology.

For comparison, the experimental data for macroscopic foams obtained through direct foaming and nanoporous foams obtained through dealloying of metal solid solutions are plotted

in Fig. 6 as well. It can be seen that these fabrication techniques produced porous materials that are stiffer, adhering more closely to the CD and CSB topologies. It is also worth noting that the stiffness of macroscopic foams changed from bending-dominated at low relative density to compression-dominated for  $\rho/\rho_s > 0.3$ , as opposed to being bending-dominated for the entire range of  $\rho/\rho_s$ , which was suggested previously [41]. Our results show that this misconception might have arose because the power law index for compression-dominated geometries increased from 1 at  $\rho/\rho_s < 0.2$  to  $\sim 2$  for  $\rho/\rho_s > 0.4$  (Table 3). While it is well-known that the power law index for bending-dominated geometries is 2 for  $E/E_s$  vs.  $\rho/\rho_s$  at low relative densities, the power law relationship for high relative density structures had not been rigorously derived previously and therefore, when it was found that the experimental value of the power law index for foams was  $\sim 2$  across the entire range of relative density, it appeared that foams were exhibiting bending-dominated deformation regardless of their porosity levels.

Using the fitted analytical data, the contributions of the various deformation modes to the overall lattice strain for each type of topology can be calculated (Fig. 7). For the FCC/ Octet Truss lattice, the only contribution to lattice strain arises from compression (*i.e.* contribution to total strain by compression = 1 for  $0 \leq \rho/\rho_s \leq 1$ ) and hence, its plot was not included in Fig. 7. For the BCC lattice, Fig. 7a shows that its relative stiffness is bending-dominated at low relative densities ( $< 0.4$ ) and shear-dominated at large relative densities. For the 3ATC lattice, its stiffness is always limited by excessive joint rotation when the relative density is varied by changing  $L$  (Fig. 6b). For the case where the relative density is varied by changing  $e$  instead, the lattice deformation is initially joint - rotation – dominated ( $\rho/\rho_s < 0.65$ ) before transitioning to compression – dominated as beams become thicker at higher relative densities ( $\rho/\rho_s > 0.8$ ) (Fig. 6b). These results are generally in line with rigorous, first principle (non-empirical) analysis of 3ATC structures [47].

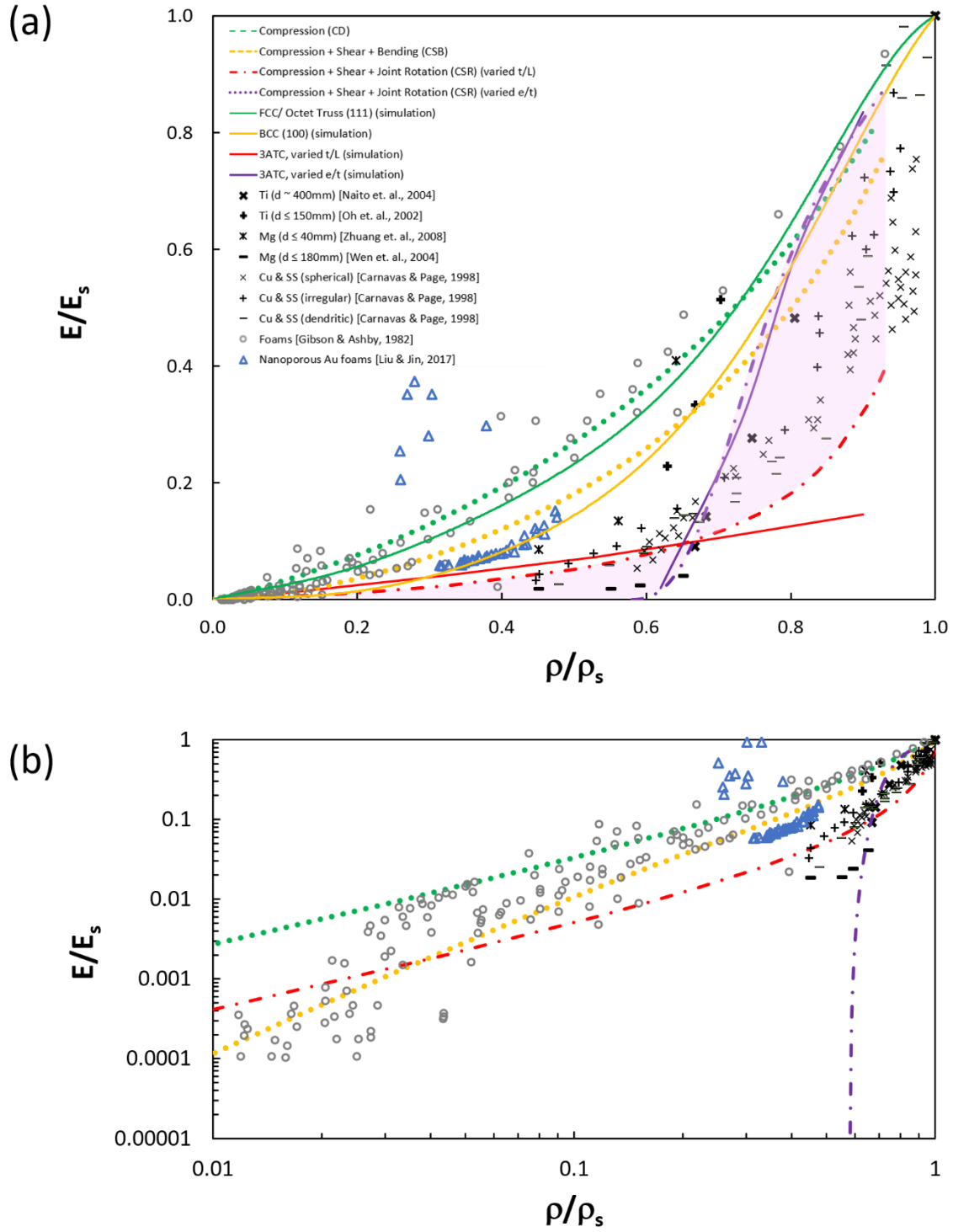


Figure 6: (a) Plot of relative stiffness,  $E/E_s$ , against relative density,  $\rho/\rho_s$ . The blue triangles and grey circles represent literature data for nanoporous foams formed by dealloying [24] and macroscopic foams formed by direct foaming [41] respectively. Literature data for powder compacted titanium (Ti) [17,54], magnesium (Mg) [21,55], copper (Cu) and stainless steel (SS) with spherical, irregular and dendritic powder morphologies ( $45 \mu\text{m} \leq d \leq 300 \mu\text{m}$ ) [31] are plotted as black data points. Solid lines represent static loading data from finite element simulations, while dashed lines represent analytical solutions. Note that for “3ATC,  $e$  varied”,

$\rho/\rho_s$  cannot reach 0 as the joint still contributes a volume of  $t^3$  to the unit cell even if the beam does not exist (*i.e.*  $e = t$ ). The fitting parameters of the analytical solutions can be found in Table 2. The region highlighted in pink covers the range of values that are possible with an 3ATC lattice geometry. (b) A log – log plot of the figure in (a).

Table 3: The value of the power law index,  $n$ , where  $y = (\rho/\rho_s)^n$ .  $y$  can be  $E/E_s$  or  $\sigma/\sigma_s$ . The values extracted from analytical trends are given without brackets while that from simulation trends are given in brackets.

Design		$\rho/\rho_s$	$n$	
			$E/E_s$	$\sigma/\sigma_s$
FCC/ Octet Truss (111)		0.4 – 0.9	1.7 (2.2)	1.4 (1.9)
BCC (100)		0.4 – 0.9	2.0 (2.1)	2.2 (2.8)
3ATC (100)	Varied $e/t$	0.6 – 0.8	14.0 (13.1)	7.0 (7.8)
	Varied $t/L$	0.4 – 0.9	3.1 (1.4)	0.9 (0.9)

Comparing Fig. 6 with Fig. 7b, it can be seen that the very low  $E/E_s$  values exhibited by the 3ATC lattices (pink region in Fig. 6) and powder compacted materials (black data points in Fig. 6) correspond to the range of relative density in Fig. 7b where joint rotation dominates, implying that joint rotation is the main cause behind the low moduli exhibited by these geometries. In contrast, when the contribution to total strain is dominated by compression or shear, in the Octet Truss and BCC lattices, as well as when  $\rho/\rho_s > 0.8$  for the 3ATC lattice (varied  $e/t$ ),  $E/E_s$  is comparatively much higher.

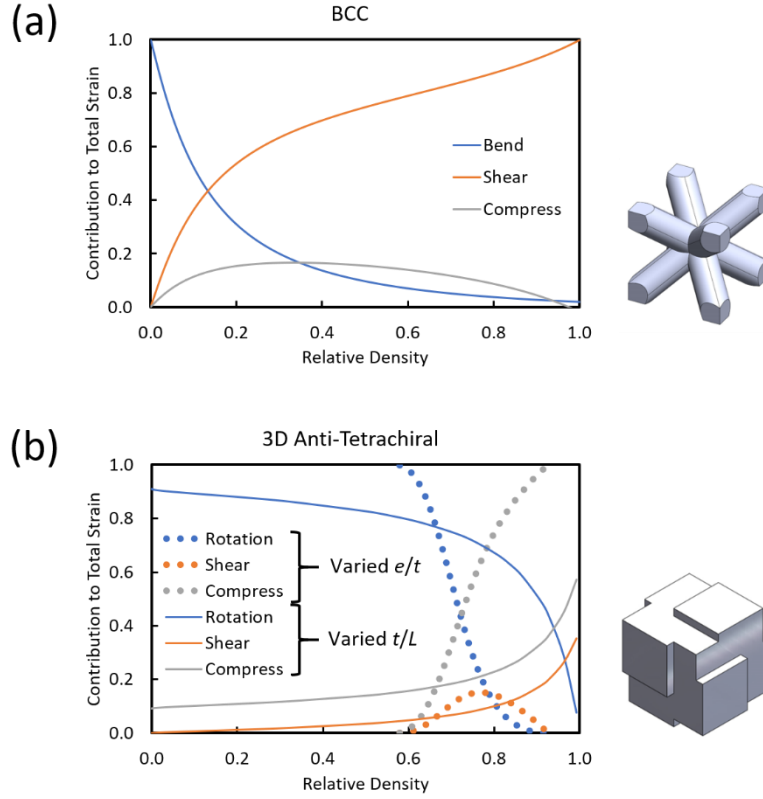


Figure 7: Respective contributions of the various deformation modes to the total strain for the (a) BCC and (c) 3ATC lattice. Note that compressive deformation is the only source of strain for FCC/ Octet Truss at all relative densities (Contribution = 1 for all  $\rho/\rho_s$ ).

### 3.2 Relative Failure Strength

Fig. 8 shows the analytical (broken lines), simulated (solid lines) and experimental (data points) values of relative strength ( $\sigma_f/\sigma_s$ ) vs. relative density ( $\rho/\rho_s$ ). As was the case with relative stiffness, the analytical trends provided a good fit with the simulated trendlines (fitting parameters shown in Table 2). Together, they suggest that the FCC lattice and by extension, the CD topology, gives the best relative strength for a given relative density, followed by the BCC lattice of CSB topology. Again, the 3ATC lattices (CSR topology) exhibited very low values of  $\sigma_f/\sigma_s$  that could not be found with CD and CSB topologies. The main exception to this lies in the low relative density regime ( $< 0.3$ ), where the relative strengths of the BCC lattice and 3ATC lattice can be comparable.



It can also be observed that majority of the experimental data points for powder compacted materials (black) are lower than the expected  $\sigma_f/\sigma_s$  values for FCC/ Octet Truss and BCC lattices, generally falling within the range for 3ATC lattices (pink region). Furthermore, the index for the power law relationship between relative strength and relative density for 3ATC lattices range from  $\sim 1 - 7$  for  $\rho/\rho_s > 0.4$  (Table 3), which is in good agreement with Hakamada *et. al.*'s previous observation of 1 - 6.3 for high relative density foams [15]. This reinforces the results obtained with relative stiffness comparisons above. Unfortunately, relative strength data for macroscopic and nanoporous foams at high relative densities ( $> 0.3$ ) are not as abundant as those for relative stiffness. Nevertheless, based on the available literature data, it appears that the foaming technique produces porous materials with microstructures that are closer to CD and CSB topologies, unlike powder compaction techniques, that lead to CSR microstructures.

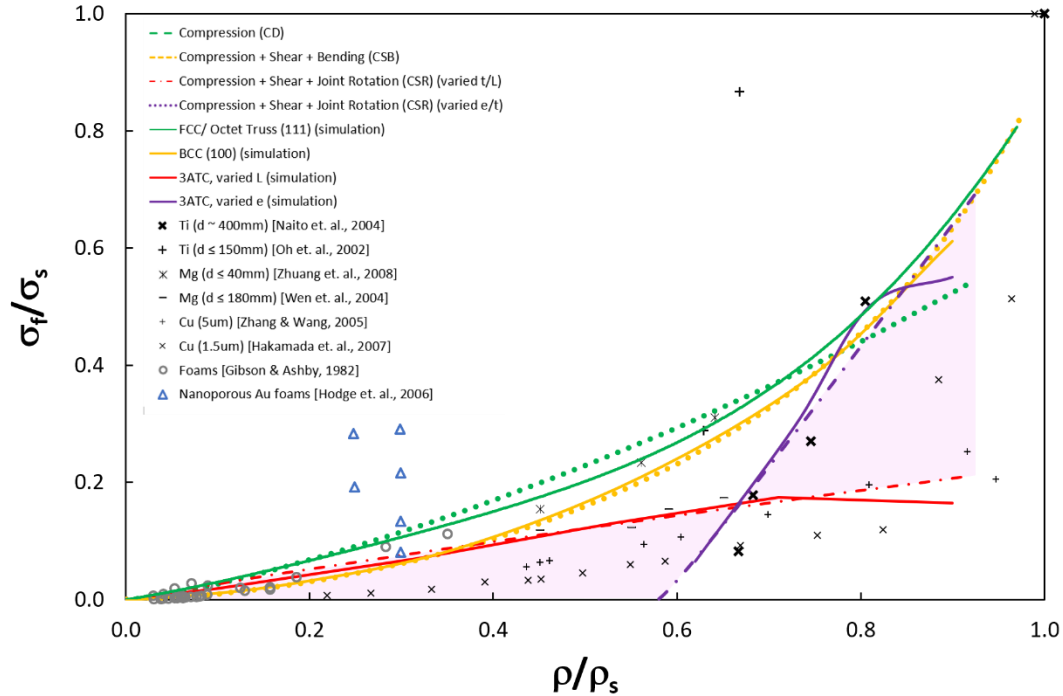


Figure 8: Plot of relative strength,  $\sigma_f/\sigma_s$ , against relative density,  $\rho/\rho_s$ . The blue triangles and grey circles represent literature data for nanoporous foams formed by dealloying [25] and macroscopic foams formed by direct foaming [41] respectively. Literature data for powder compacted titanium (Ti) [17,54], magnesium (Mg) [21,55] and copper (Cu) [15,56] are plotted as black data points. Solid lines represent static loading data from finite element simulations,

while broken lines represent analytical solutions. Note that for “3ATC,  $e$  varied”,  $\rho/\rho_s$  cannot reach 0 as the joint still contributes a volume of  $t^3$  to the unit cell even if the beam does not exist (*i.e.*  $e = t$ ). The fitting parameters of the analytical solutions can be found in Table 3. The region highlighted in pink covers the range of relative strength values that are possible with an 3ATC lattice geometry.

Breaking down the respective contributions by the various deformation modes to total stress, it can be observed that, at extremely low relative densities ( $< 0.01$ ), the lattice strength of FCC/ Octet Truss is limited by bending stresses arising from beam buckling (Fig. 9a). For larger relative densities, bending and compressive stresses co-dominate, with compressive stresses becoming more important as  $\rho/\rho_s$  rises. This is expected, as thicker beams at higher relative densities are less prone to buckling and bending.

For the BCC lattice, it is interesting to note that the bending stress is much larger than that of shear or compression for the full range of relative density (Fig. 9b), although increasingly thick beams at higher relative densities did improve the contribution of the compressive stress to the total stress. Shear stress, on the other hand, remains very much negligible regardless of the relative density. This may seem to run counter to the observation above that shear is the main cause of BCC lattice strain for  $\rho/\rho_s > 0.4$ , but as seen from the case of Octet Truss at low relative density ( $< 0.01$ ), the deformation mode that determines the lattice strain and strength may not necessarily be the same [43]. In addition, it should be noted that, unlike the case of Octet Truss and 3ATC lattices, the maximum stress experienced by an element in a BCC lattice is not a simple sum of all the stresses. Instead, it is dictated by the difference between the compressive and bending stresses and its relative magnitude with respect to the shear stress, as governed by Mohr’s circle (Eq. (29)).

For the 3ATC lattice, it is clear that compressive stress is the limiting determinant of lattice stress across all relative densities, except for a very small range of  $0.58 < \rho/\rho_s \leq 0.59$  for 3ATC ( $e$  varied), where compressive and bending stresses had similar values (Fig. 9c). Despite being compression-limited, the relative strength of 3ATC lattices for a given relative density

is much lower compared to that of an Octet Truss lattice (Fig. 8). This is because, for the given joint size of  $t \times t \times t$ , the effective loading area for a beam in an 3ATC lattice,  $(t - e)^2$ , is lower than that of an Octet Truss lattice,  $t^2$ . This leads to higher stresses in 3ATC beams and consequently, failure at smaller external loads compared to the Octet Truss. Powder compacted porous materials probably exhibit similar  $\sigma/\sigma_s$  values as 3ATC lattices for the same reason – the neck-like interparticle connections that act as beams usually have significantly smaller cross-sectional areas than the particulate joints [57,58].

It is also interesting to note in Fig. 9c that the trends for compression and bending contributions to the total stress of 3ATC ( $t/L$  varied) are constant. This can be understood from Eq. (44) and (45), which can be combined to give

$$\frac{\sigma_{stretch}}{\sigma_{bend}} \propto (t - e) , \quad (47)$$

demonstrating that the value of  $\sigma_{stretch}$ , with respect to  $\sigma_{bend}$ , is independent of  $L$ .

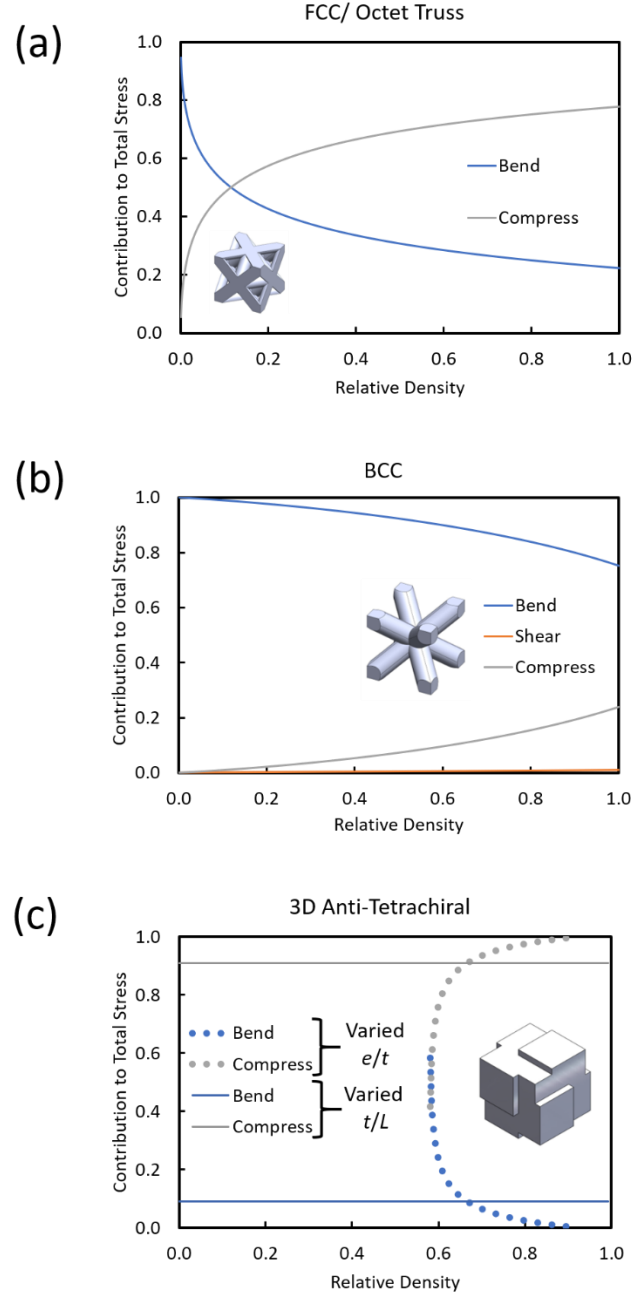


Figure 9: Respective contributions of the various deformation modes to the total stress for the (a) FCC/ Octet Truss (b) BCC and (c) 3ATC lattice.

#### 4. DISCUSSION

The results presented above strongly suggests that rotation of joints, which were originally particles before compaction, is the main cause behind the small elastic moduli of porous materials fabricated through powder compaction. The load bearing inefficiency of these

eccentric CSR microstructures lies with the fact that most of the material is gathered in the joint rather than in the beams (*i.e.* the neck-like interparticle connections) where it may help restrict the rotation of the joint. The relatively large size of the joints also means that small loads can potentially cause large moments and rotations, which lead to large lattice strains for powder compacted materials. The highly uneven distribution of material between the joints and struts is also the main reason for the much lower relative strength of these structures, as the stresses become heightened in the narrow interparticle necks, which are the weak links in the structure.

These inferences are further supported by tomographic images of powder compacted materials from multiple studies (Fig. 10a – 10d), which clearly show that the majority of particles are eccentrically attached to their neighbours (red) with only a few symmetrical exceptions (green). In addition, experimental observations of particle rotations during the compression of granular/ powder materials are also well-documented in previous studies [59–61]. One study, in particular, noted that higher coordination numbers led to reduced particulate rotation during loading [61], which is consistent with the geometries used in this study – Octet Truss and BCC have coordination numbers of 12 and 8 respectively and are symmetric, while the asymmetric 3ATC structure has the lowest coordination number of 6.

The reason for this relationship between coordination number and joint rotation is illustrated in Fig. 10e and 10f. If a 2D circle has a coordination number of 2, there is only 1 configuration where no moment or rotation of the central particle (in green) would be generated (Fig. 10e). However, if the coordination number is now increased to 3, the third particle can attach anywhere along the red border of the central particle and cause a reduction of the original moment caused by the prior 2 particles (Fig. 10f). Qualitatively, from Fig. 10f, we can see that there is a more than fair chance of that happening since the red border takes up nearly all of the remaining circumference of the central particle that is available for attachment. Extrapolating this to 3D space, we can therefore expect a higher coordination number to reduce particle

rotation because the eccentric positioning of neighbours around a particle has a tendency to be cancelled out with increasing number of neighbouring particles *i.e.* it is extremely unlikely that all the attachments will contribute towards the same moment vector.

The strategy for improving the stiffness of powder compacted porous materials is, therefore, to increase the packing density as much as possible prior to compaction, so that particle arrangement approaches that of the Octet Truss or BCC design (high coordination number), rather than the random loose pack structure (low coordination number). Previous studies have shown that this can be achieved through the use of vibrations during compaction [62] or lubricants to reduce interparticle friction [63].

As for improving the strength of powder compacted materials, the interparticle connections have to be thickened with increased compressive pressure [36], higher sintering temperatures [64] and/ or longer compaction times [57]. These approaches have already been attempted and shown to work, but it should be noted that they, together with strategies to increase packing density, would decrease porosity, which may be undesirable if very low relative density materials are required.

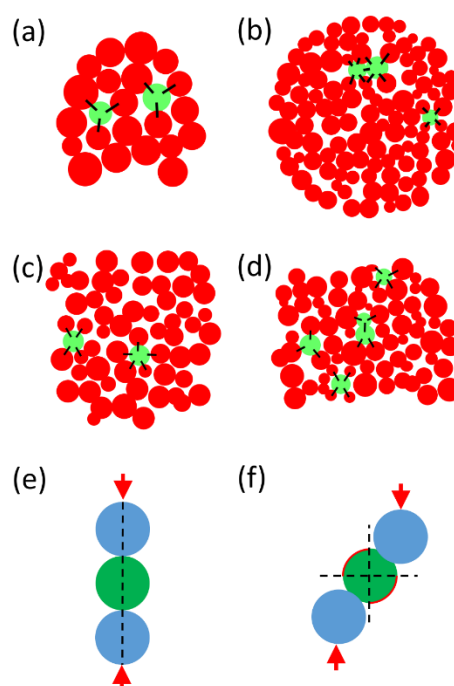


Figure 10: Illustration of experimentally and numerically obtained 2D slices in 3D powder compacted (a) copper ( $\rho/\rho_s = 0.7$ ) [61] (b) copper ( $\rho/\rho_s = 0.72$ ) [65] (c) glass ( $\rho/\rho_s = 0.65$ ) [57] and (d) copper ( $\rho/\rho_s$  not given) [58]. Red - particles with eccentrically arranged neighbours. Green - particles with approximately symmetric connections. Black lines highlight these interparticle connections. Schematic illustration of (e) a non-eccentric arrangement of 3 particles (f) an eccentric arrangement of particles about the center particle (green). The red arrows represent external forces and the red border of the center particle (green) highlight the sites where a 3<sup>rd</sup> particle can attach in order to reduce the moment and rotation of the center particle caused by the first 2 eccentrically positioned particles.

## 5. CONCLUSIONS

The microstructural cause behind the weak mechanical properties exhibited by porous powder compacted materials was investigated in this study. Comparing experimental data of stiffness and strength previously reported for powder compacted materials against the trendlines obtained from finite element simulations and analytical solutions derived for the compression/ stretch – dominated (CD), compression, shear and bending (CSB) and compression, shear and joint rotation (CSR) topologies, we found that eccentric geometries and accompanying joint/ particle rotation, as well as narrow neck-like interparticle connections, were the main reasons behind the low modulus and strength of powder compacted porous materials. This result is supported by numerous reports documenting the eccentricity of the microstructures in such materials, as well as measurements of particulate rotation during compression tests. This insight also implies that the packing density of the powder has to be increased as much as possible before compaction in order to reduce the geometrical eccentricity and particle rotation in the microstructures, which would lead to better stiffness for the porous powder compacted materials. The material strength, on the other hand, can be improved through thickening of the interparticle connections using a higher temperature, compressive pressure and/ or compaction duration.

## ACKNOWLEDGEMENTS

Funding for this project was provided by C.Q.L.'s Temasek Research Fellowship, for which he gives thanks.

## REFERENCES

- [1] Meza LR, Zelhofer AJ, Clarke N, Mateos AJ, Kochmann DM, Greer JR. Resilient 3D hierarchical architected metamaterials. *Proc Natl Acad Sci* 2015;112:11502–7. <https://doi.org/10.1073/pnas.1509120112>.
- [2] Schaedler TA, Jacobsen AJ, Torrents A, Sorensen AE, Lian J, Greer JR, et al. Ultralight Metallic Microlattices. *Science* 2011;334:962–5. <https://doi.org/10.1126/science.1211649>.
- [3] Zheng X, Lee H, Weisgraber TH, Shusteff M, DeOtte J, Duoss EB, et al. Ultralight, ultrastiff mechanical metamaterials. *Science* 2014;344:1373–7. <https://doi.org/10.1126/science.1252291>.
- [4] Deshpande VS, Fleck NA, Ashby MF. Effective properties of the octet-truss lattice material. *J Mech Phys Solids* 2001;49:1747–69. [https://doi.org/10.1016/S0022-5096\(01\)00010-2](https://doi.org/10.1016/S0022-5096(01)00010-2).
- [5] Yap XY, Seetoh I, Goh WL, Ye P, Zhao Y, Du Z, et al. Mechanical properties and failure behaviour of architected alumina microlattices fabricated by stereolithography 3D printing. *Int J Mech Sci* 2021;196:106285. <https://doi.org/10.1016/j.ijmecsci.2021.106285>.
- [6] Kanaujia PK, bin Ramezan MA, Yap XY, Song Y, Du Z, Gan CL, et al. Mechanical response of lightweight hollow truss metal oxide lattices. *Materialia* 2019;8:100439. <https://doi.org/10.1016/j.mtla.2019.100439>.
- [7] Bouix R, Viot P, Lataillade J-L. Polypropylene foam behaviour under dynamic loadings: Strain rate, density and microstructure effects. *Int J Impact Eng* 2009;36:329–42. <https://doi.org/10.1016/j.ijimpeng.2007.11.007>.
- [8] Chen W, Lu F, Winfree N. High-strain-rate compressive behavior of a rigid polyurethane foam with various densities. *Exp Mech* 2002;42:65–73. <https://doi.org/10.1007/BF02411053>.
- [9] Lai CQ, Daraio C. Highly Porous Microlattices as Ultrathin and Efficient Impact Absorbers. *Int J Impact Eng* 2018;120:138–49.
- [10] Han F, Seiffert G, Zhao Y, Gibbs B. Acoustic absorption behaviour of an open-celled aluminium foam. *J Phys Appl Phys* 2003;36:294. <https://doi.org/10.1088/0022-3727/36/3/312>.
- [11] Gibson LJ, Ashby MF. *Cellular Solids: Structure and Properties*. 2 edition. Cambridge: Cambridge University Press; 1999.
- [12] Ashby MF. The properties of foams and lattices. *Philos Trans R Soc Lond Math Phys Eng Sci* 2006;364:15–30. <https://doi.org/10.1098/rsta.2005.1678>.
- [13] Valdevit L, Jacobsen AJ, Greer JR, Carter WB. Protocols for the Optimal Design of Multi-Functional Cellular Structures: From Hypersonics to Micro-Architected Materials. *J Am Ceram Soc* 2011;94:s15–34. <https://doi.org/10.1111/j.1551-2916.2011.04599.x>.
- [14] Cuevas FG, Montes JM, Cintas J, Urban P. Electrical conductivity and porosity relationship in metal foams. *J Porous Mater* 2009;16:675. <https://doi.org/10.1007/s10934-008-9248-1>.
- [15] Hakamada M, Asao Y, Kuromura T, Chen Y, Kusuda H, Mabuchi M. Density dependence of the compressive properties of porous copper over a wide density range. *Acta Mater* 2007;55:2291–9. <https://doi.org/10.1016/j.actamat.2006.11.024>.
- [16] Jana DC, Sundararajan G, Chattopadhyay K. Effect of Porosity on Structure, Young's Modulus, and Thermal Conductivity of SiC Foams by Direct Foaming and Gelcasting. *J Am Ceram Soc* 2017;100:312–22. <https://doi.org/10.1111/jace.14544>.



- [17] Oh I-H, Nomura N, Hanada S. Microstructures and Mechanical Properties of Porous Titanium Compacts Prepared by Powder Sintering. *Mater Trans* 2002;43:443–6.
- [18] Zhao L, Lam YC, Lai CQ. Interaction of ultrasound with microporous polyethylene scaffolds. *Appl Acoust* 2019;153:102–9. <https://doi.org/10.1016/j.apacoust.2019.04.007>.
- [19] Frodel JL, Lee S. The Use of High-Density Polyethylene Implants in Facial Deformities. *Arch Otolaryngol Neck Surg* 1998;124:1219–23. <https://doi.org/10.1001/archotol.124.11.1219>.
- [20] Lee S, Maronian N, Most SP, Whipple ME, McCulloch TM, Stanley RB, et al. Porous High-Density Polyethylene for Orbital Reconstruction. *Arch Otolaryngol Neck Surg* 2005;131:446–50. <https://doi.org/10.1001/archotol.131.5.446>.
- [21] Zhuang H, Han Y, Feng A. Preparation, mechanical properties and in vitro biodegradation of porous magnesium scaffolds. *Mater Sci Eng C* 2008;28:1462–6. <https://doi.org/10.1016/j.msec.2008.04.001>.
- [22] Pokhrel A, Seo DN, Lee ST, Kim IJ, Pokhrel A, Seo DN, et al. Processing of Porous Ceramics by Direct Foaming: A Review. *J Korean Ceram Soc* n.d.;50:93. <https://doi.org/2013.50.2.93>.
- [23] Deng X, Wang J, Du S, Li F, Lu L, Zhang H. Fabrication of Porous Ceramics by Direct Foaming. *Interceram - Int Ceram Rev* 2014;63:104–8. <https://doi.org/10.1007/BF03401041>.
- [24] Liu L-Z, Jin H-J. Scaling equation for the elastic modulus of nanoporous gold with “fixed” network connectivity. *Appl Phys Lett* 2017;110:211902. <https://doi.org/10.1063/1.4984108>.
- [25] Hodge AM, Biener J, Hayes JR, Bythrow PM, Volkert CA, Hamza AV. Scaling equation for yield strength of nanoporous open-cell foams. *Acta Mater* 2007;55:1343–9. <https://doi.org/10.1016/j.actamat.2006.09.038>.
- [26] Merkt S, Hinke C, Bültmann J, Brandt M, Xie YM. Mechanical response of TiAl6V4 lattice structures manufactured by selective laser melting in quasistatic and dynamic compression tests. *J Laser Appl* 2014;27:S17006. <https://doi.org/10.2351/1.4898835>.
- [27] Körner C. Additive manufacturing of metallic components by selective electron beam melting — a review. *Int Mater Rev* 2016;61:361–77. <https://doi.org/10.1080/09506608.2016.1176289>.
- [28] Markandan K, Lai CQ. Enhanced mechanical properties of 3D printed graphene-polymer composite lattices at very low graphene concentrations. *Compos Part Appl Sci Manuf* 2020;129:105726. <https://doi.org/10.1016/j.compositesa.2019.105726>.
- [29] Seetoh I, Markandan K, Lai CQ. Effect of reinforcement bending on the elastic properties of interpenetrating phase composites. *Mech Mater* 2019;136:103071. <https://doi.org/10.1016/j.mechmat.2019.103071>.
- [30] Markandan K, Lim R, Kumar Kanaujia P, Seetoh I, bin Mohd Rosdi MR, Tey ZH, et al. Additive manufacturing of composite materials and functionally graded structures using selective heat melting technique. *J Mater Sci Technol* 2020;47:243–52. <https://doi.org/10.1016/j.jmst.2019.12.016>.
- [31] Carnavas PC, Page NW. Elastic properties of compacted metal powders. *J Mater Sci* 1998;33:4647–55. <https://doi.org/10.1023/A:1004445527430>.
- [32] Fang ZZ, Paramore JD, Sun P, Chandran KSR, Zhang Y, Xia Y, et al. Powder metallurgy of titanium – past, present, and future. *Int Mater Rev* 2018;63:407–59. <https://doi.org/10.1080/09506608.2017.1366003>.
- [33] Merhar J. Overview of metal injection moulding. *Met Powder Rep* 1990;45:339–42. [https://doi.org/10.1016/S0026-0657\(10\)80242-5](https://doi.org/10.1016/S0026-0657(10)80242-5).
- [34] Hangai Y, Yoshida H, Yoshikawa N. Friction Powder Compaction for Fabrication of Open-Cell Aluminum Foam by the Sintering and Dissolution Process Route. *Metall Mater Trans A* 2012;43:802–5. <https://doi.org/10.1007/s11661-011-1073-5>.
- [35] Xiao D, Yuan T, Ou X, He Y. Microstructure and mechanical properties of powder metallurgy Ti-Al-Mo-V-Ag alloy. *Trans Nonferrous Met Soc China* 2011;21:1269–76. [https://doi.org/10.1016/S1003-6326\(11\)60852-2](https://doi.org/10.1016/S1003-6326(11)60852-2).
- [36] Atkinson HV, Davies S. Fundamental aspects of hot isostatic pressing: An overview. *Metall Mater Trans A* 2000;31:2981–3000. <https://doi.org/10.1007/s11661-000-0078-2>.

- [37] Irukuvarghula S, Hassanin H, Cayron C, Aristizabal M, Attallah MM, Preuss M. Effect of powder characteristics and oxygen content on modifications to the microstructural topology during hot isostatic pressing of an austenitic steel. *Acta Mater* 2019;172:6–17. <https://doi.org/10.1016/j.actamat.2019.03.038>.
- [38] Xie F, He X, Ji X, Wu M, He X, Qu X. Structural characterisation and mechanical behaviour of porous Ti-7.5Mo alloy fabricated by selective laser sintering for biomedical applications. *Mater Technol* 2017;32:219–24. <https://doi.org/10.1080/10667857.2016.1173169>.
- [39] Wen P, Jauer L, Voshage M, Chen Y, Poprawe R, Schleifenbaum JH. Densification behavior of pure Zn metal parts produced by selective laser melting for manufacturing biodegradable implants. *J Mater Process Technol* 2018;258:128–37. <https://doi.org/10.1016/j.jmatprotec.2018.03.007>.
- [40] Dadbakhsh S, Verbelen L, Vandeputte T, Strobbe D, Van Puyvelde P, Kruth J-P. Effect of Powder Size and Shape on the SLS Processability and Mechanical Properties of a TPU Elastomer. *Phys Procedia* 2016;83:971–80. <https://doi.org/10.1016/j.phpro.2016.08.102>.
- [41] Gibson IJ, Ashby MF. The mechanics of three-dimensional cellular materials. *Proc R Soc Lond A* 1982;382:43–59. <https://doi.org/10.1098/rspa.1982.0088>.
- [42] Wang JC. Young's modulus of porous materials. *J Mater Sci* 1984;19:809–14. <https://doi.org/10.1007/BF00540452>.
- [43] He Z, Wang F, Zhu Y, Wu H, Park HS. Mechanical properties of copper octet-truss nanolattices. *J Mech Phys Solids* 2017;101:133–49. <https://doi.org/10.1016/j.jmps.2017.01.019>.
- [44] Hoogenboom JP, Rétif C, de Bres E, van de Boer M, van Langen-Suurling AK, Romijn J, et al. Template-Induced Growth of Close-Packed and Non-Close-Packed Colloidal Crystals during Solvent Evaporation. *Nano Lett* 2004;4:205–8. <https://doi.org/10.1021/nl034867h>.
- [45] Manoharan VN. Colloidal matter: Packing, geometry, and entropy. *Science* 2015;349:1253751. <https://doi.org/10.1126/science.1253751>.
- [46] Woodcock LV. Entropy difference between the face-centred cubic and hexagonal close-packed crystal structures. *Nature* 1997;385:141–3. <https://doi.org/10.1038/385141a0>.
- [47] Lai CQ, Markandan K, Lu Z. Anomalous elastic response of a 3D anti - tetrachiral metamaterial. *Int J Mech Sci* 2021;192:106142. <https://doi.org/10.1016/j.ijmecsci.2020.106142>.
- [48] Blodgett OW. Design of Welded Structures with Welding Safety and Welding Resources DVDs. James F. Lincoln Arc Welding Foundation; 2016.
- [49] Carrera E, Giunta G, Petrolo M. Beam Structures: Classical and Advanced Theories. 1 edition. Chichester, West Sussex, U.K: Wiley; 2011.
- [50] Beer F, Johnston Jr ER, DeWolf J, Mazurek D. Mechanics of Materials. 6th ed. McGraw-Hill Science/Engineering/Math; 2011.
- [51] Chen W-F, Zhang H. Structural plasticity: theory, problems, and CAE software. Springer-Verlag; 1991.
- [52] Bertoldi K, Reis PM, Willshaw S, Mullin T. Negative Poisson's Ratio Behavior Induced by an Elastic Instability. *Adv Mater* 2010;22:361–6. <https://doi.org/10.1002/adma.200901956>.
- [53] Sullivan RM, Ghosn LJ, Lerch BA. A general tetrakaidecahedron model for open-celled foams. *Int J Solids Struct* 2008;45:1754–65. <https://doi.org/10.1016/j.ijsolstr.2007.10.028>.
- [54] Naito Y, Bae J, Tomotake Y, Hamada K, Asaoka K, Ichikawa T. Formability and mechanical properties of porous titanium produced by a moldless process. *J Biomed Mater Res B Appl Biomater* 2013;101:1090–4. <https://doi.org/10.1002/jbm.b.32919>.
- [55] Wen CE, Yamada Y, Shimojima K, Chino Y, Hosokawa H, Mabuchi M. Compressibility of porous magnesium foam: dependency on porosity and pore size. *Mater Lett* 2004;58:357–60. [https://doi.org/10.1016/S0167-577X\(03\)00500-7](https://doi.org/10.1016/S0167-577X(03)00500-7).
- [56] Zhang E, Wang B. On the compressive behaviour of sintered porous coppers with low to medium porosities—Part I: Experimental study. *Int J Mech Sci* 2005;47:744–56. <https://doi.org/10.1016/j.ijmecsci.2004.12.011>.

- [57] Bernard D, Gendron D, Heintz J-M, Bordère S, Etourneau J. First direct 3D visualisation of microstructural evolutions during sintering through X-ray computed microtomography. *Acta Mater* 2005;53:121–8. <https://doi.org/10.1016/j.actamat.2004.09.027>.
- [58] Lame O, Bellet D, Di Michiel M, Bouvard D. Bulk observation of metal powder sintering by X-ray synchrotron microtomography. *Acta Mater* 2004;52:977–84. <https://doi.org/10.1016/j.actamat.2003.10.032>.
- [59] Druckrey Andrew M., Alshibli Khalid A. 3D Behavior of Sand Particles Using X-Ray Synchrotron Micro-Tomography. *Geo-Congr 2014 Tech Pap* n.d.:2814–21. <https://doi.org/10.1061/9780784413272.272>.
- [60] Dai B, Liu C, Lan L, Chen H. Study on Internal Structure and Deformation Features of Polymer Bonded Explosives Particles during Compression Process by In-situ Micro-computed Tomography Imaging and Digital Volume Correlation Method, Singapore: 2017.
- [61] McDonald SA, Holzner C, Lauridsen EM, Reischig P, Merkle AP, Withers PJ. Microstructural evolution during sintering of copper particles studied by laboratory diffraction contrast tomography (LabDCT). *Sci Rep* 2017;7. <https://doi.org/10.1038/s41598-017-04742-1>.
- [62] Rémond S, Gallias JL. Simulation of periodic mono-sized hard sphere systems under different vibration conditions and resulting compaction. *Phys Stat Mech Its Appl* 2006;369:545–61. <https://doi.org/10.1016/j.physa.2006.01.071>.
- [63] Yang S-D, Zhang R-J, Qu X-H. X-ray tomography analysis of aluminum alloy powder compaction. *Rare Met* 2015. <https://doi.org/10.1007/s12598-015-0628-9>.
- [64] Wright JK. The effect of firing conditions on the Strength of Hematite compacts. *Powder Technol* 1976;14:103–13. [https://doi.org/10.1016/0032-5910\(76\)80012-5](https://doi.org/10.1016/0032-5910(76)80012-5).
- [65] Tikare V, Braginsky M, Bouvard D, Vagnon A. Numerical simulation of microstructural evolution during sintering at the mesoscale in a 3D powder compact. *Comput Mater Sci* 2010;48:317–25. <https://doi.org/10.1016/j.commatsci.2010.01.013>.